J. Plasma Phys. (2022), *vol*. 88, 905880316
Published by Cambridge University Press

doi:10.1017/S0022377822000538

Optical diagnosis of a kHz-driven helium atmospheric pressure plasma jet

C. McDonnell[1], R. Irwin[1], S. White[1], W.G. Graham[1] and D. Riley[1]

[1]Centre for Plasma Physics, School of Maths and Physics, Queen's University Belfast, BT7 1NN Belfast, UK

(Received 30 March 2022; revised 30 May 2022; accepted 1 June 2022)

This paper focuses on utilizing several different optical diagnostics to experimentally characterize a pure helium atmospheric pressure plasma jet. Axial electric field measurements were carried out along the plasma plume through the use of a non-perturbing method based on polarization-dependent Stark spectroscopy of the helium 492.2 nm line. The electric field is shown to increase with distance along the plume length, reaching values as high as 24.5 kV cm^{-1}. The rate of increase of the electric field is dependent on the helium gas flow rate, with lower gas flows rising quicker with distance in comparison with larger flow rates, with the typical values remaining within the same range. This sensitivity is linked to gas mixing between the helium and surrounding ambient air. Schlieren imaging of the gas flow is included to support this. The addition of a target is shown to further increase the measured electric field in close range to the target, with the magnitude of this increase being strongly dependent on the distance between the tube exit and target. The relative increase in the electric field is shown to be on average greater for a conducting target of water in comparison with plastic. A minimal equipment optical configuration, which is here referred to as fast two-dimensional monochromatic imaging, is introduced as an approach for estimating excited state densities within the plasma. Densities of the upper helium states for transitions, $1s3s\ ^3S_1 \rightarrow 1s2p\ ^3P^0_{0,1,2}$ at 706.5 nm and $1s3s\ ^1S_0 \rightarrow 1s2p\ ^1P^0_1$ at 728.1 nm, were estimated using this approach and found to be of the order of 10^{10}–10^{11} cm^{-3}.

Key words: plasma diagnostics, electric discharges, plasma applications

1. Introduction

Atmospheric pressure plasma jets (APPJs) have been widely studied in recent decades. Their low gas temperature and abundance of highly reactive chemical species make them ideal candidates for a number of particular applications such as medical (Park *et al.* 2012), surface sterilization (Laroussi *et al.* 2012) and agricultural (Attri *et al.* 2020). Operating at atmospheric pressure provides many benefits such as a lower cost plus simplicity and flexibility to set up, as there is no need for the vacuum systems commonly needed for low pressure plasmas. However, this makes understanding the plasma chemistry much more difficult as the surrounding environment is no longer controlled and collisional reactions

with ambient air now play a dominant role. To optimize the performance of APPJs to suit the particular application, it is important to know the properties of the plasma such as the reactive species density, electron density and temperature and in particular how varying controllable parameters such as the gas flow and applied voltage may affect these properties.

One of the most important properties from the point of view of biological applications is the electric field produced by the plasma jet. If the field is high enough, cell electroporation may be achieved, temporarily creating pore-like openings in the cell membrane. This makes it much easier for reactive species produced by the plasma jet source to successfully penetrate the membrane and enter the cell (Kim *et al.* 2010; Zhang *et al.* 2014). One study of HL-60 cells indicates that a threshold of $30\,\mathrm{kV\,cm^{-1}}$ for 60 ns duration is sufficient to achieve cell electroporation (Beebe *et al.* 2004). Another study conducted on skin tumour cells, investigated the application of nanosecond pulsed electric fields of greater than $20\,\mathrm{kV\,cm^{-1}}$ and found that the cell nuclei shrunk and caused blood flow to the tumours to stop (Nuccitelli *et al.* 2006). This magnitude of electric field is obtainable for the plasma jet source discussed in this work. Previous biological studies conducted using our plasma jet device exhibit its potential applications for the sterilization of bacteria cells (Flynn *et al.* 2016) and the detoxification of maize (Wielogorska *et al.* 2019), which provides a strong motivation to study the physical conditions within our particular jet. Many of the APPJs studied in the literature have different geometries, electrode configurations and power delivery, hence direct reproducibility between plasma jets cannot always be made. Having a combined knowledge of both the physical and biological nature of these individually unique APPJs can therefore help further expand the existing knowledge.

For all applications of these types of plasma jet sources, the plasma plume interacts with some form of target. This could be a metallic surface being treated/decontaminated or a wound being disinfected. It is now well known that any object in close vicinity of the plasma plume will change the dynamics of the plasma (Akishev *et al.* 2017; Kovačević *et al.* 2018; Sobota *et al.* 2019). The addition of a target has already been shown to increase helium metastable densities (Urabe *et al.* 2010; Zaplotnik *et al.* 2016) and electron densities in close proximity to the target (Klarenaar *et al.* 2018; Hofmans *et al.* 2020; Viegas *et al.* 2020). It is therefore essential to study the plasma under different target conditions similar to those of their particular application to get a better understanding of the typical plasma behaviour and properties. This work highlights the sensitivity of the axial electric field along the plasma plume to changes of the parameters such as the helium gas flow rate, target properties and the separation between the target and tube exit.

Another important property of APPJs is their ability to produce a wide variety of reactive and excited species. One of the primary goals for APPJs within this decade has been to develop diagnostic methods capable of measuring densities of excited species, metastable states and reactive species (Lu *et al.* 2014). Concentrations of reactive species such as O, OH and NO can be determined experimentally through the use of one- or two-photon laser-induced fluorescence spectroscopy and optical absorption spectroscopy (van Gessel, Alards & Bruggeman 2013; Pei *et al.* 2014; Yonemori & Ono 2014; Xiong, Yang & Bruggeman 2015; Schröter *et al.* 2020; Steuer *et al.* 2021). However, few experimental studies have focused on measuring the density of excited species. This work estimates excited state densities within the plasma directly from plasma emission without the need for a laser and complex optics, hence making it a cheaper and simpler method. By spectrally isolating emission through the use of a bandpass filter coupled to a calibrated intensified CCD (iCCD) camera, images of the plasma bullets can be analysed and used to determine temporal and spatially resolved excited state densities. One advantage of this compact experimental configuration is that it provides the capability

https://doi.org/10.1017/S0022377822000538 Published online by Cambridge University Press

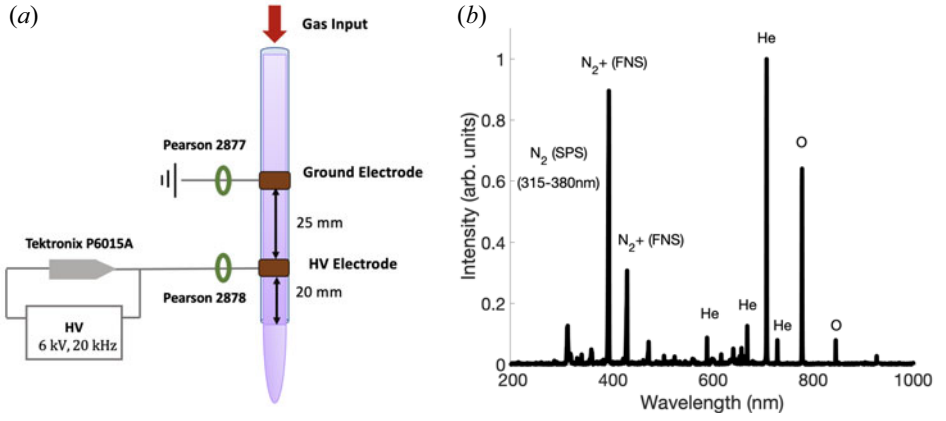

FIGURE 1. (*a*) Schematic of the plasma jet source used in this work. The jet is vertically orientated with the helium gas flow represented by the arrow and (*b*) typical spectrum of the excited species produced by this plasma jet source taken along the plume at 1 mm from the tube exit.

of having multi-diagnostic measurements. For example, electric field measurements and excited state density measurements could be conducted simultaneously, assuming one has access to two iCCD cameras, although this was not the case for the work presented here. The ability to make multi-diagnostic measurements can be a very useful tool due to the sensitivity of APPJs where streamer propagation and the plasma bullets temporal and spatial position is not always completely reproducible (Xian *et al.* 2009; Wu, Lu & Pan 2013; Lu *et al.* 2014).

2. Experimental set-up

The plasma jet used in this study is a form of dielectric barrier discharge produced by our custom built apparatus, the plasma jet source. The plasma jet source consists of two copper ring electrodes, each 5 mm wide and 100 μm thick, wrapped externally around a cylindrical quartz tube (inner diameter: 4 mm outer diameter: 6 mm) vertically orientated as depicted in figure 1(*a*). The powered electrode is fixed at a distance of 20 mm from the exit nozzle of the tube and remains separated from the grounded electrode at a distance of 25 mm. To ignite the plasma, a high voltage (1–12 kV) pulsed power supply (Haiden PHF-2 K) with repetition rates in the 1–100 kHz range is applied between the two electrodes and helium gas (99.9 % purity) is passed through the tube and a stream of plasma bullets are produced. The plasma plume extends into open air at atmospheric pressure and room temperature. The applied voltage is measured using a Tekronix P6015A high voltage probe and two Pearson probes monitor the current in both the powered and grounded cable. The voltage pulse is attenuated by the probe by 1000x before being viewed via a GHz digital oscilloscope (Tektronix TDS5104). Typical voltage and current waveforms are shown in figure 2 for a supplied voltage of 6 kV at a repetition frequency of 20 kHz and a helium flow rate of 2 standard litres per minute (slm). The spike in the ground current at approximately 3 μs corresponds to the plasma breakdown. Plasma bullets are generated only in this first positive half-cycle of the voltage waveform and last several hundreds of nanoseconds, reaching peak velocities of up to 100 km s^{-1}.

An example of the excited species produced by the plasma is presented in figure 1(*b*). This spectrum was taken along the plume at 1 mm from the tube exit using an Ocean Optics broadband USB spectrometer. Several helium lines are identified, the most

https://doi.org/10.1017/S0022377822000538 Published online by Cambridge University Press

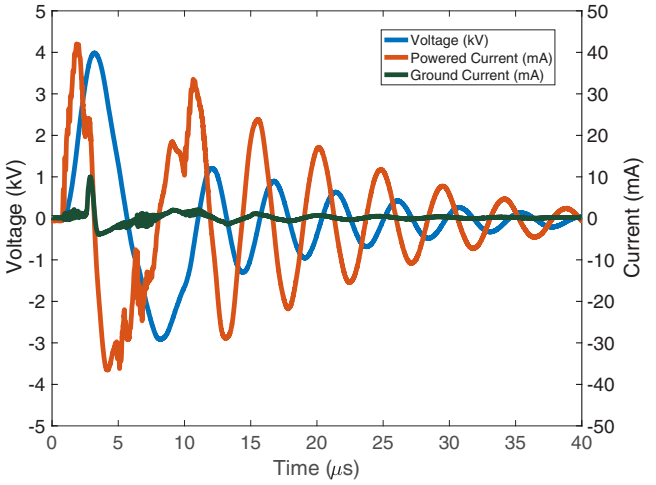

FIGURE 2. Waveform profiles of the applied voltage (blue) and current (orange) flowing through the powered electrode, and the current flowing through the ground electrode (green) (6 kV, 2 slm, 20 kHz).

intense being the helium 706.5 nm line, which is an indication of high energy electrons (Walsh *et al.* 2010). The presence of atomic oxygen can be seen from emission at the 777.4 nm triplet and 844.7 nm singlet and is often desirable for plasma related biomedical applications due to its effective sterilization ability (Moreau, Orange & Feuilloley 2008; Kong *et al.* 2009; Georgescu *et al.* 2010). Multiple nitrogen lines are also present, with strong emission from the excited ions, N_2^+, produced predominately by Penning ionization between ground state nitrogen and helium metastables (Sretenovic *et al.* 2012).

3. Results and discussion

3.1. *Electric field measurements*

A non-perturbing spectroscopic method was used to measure the electric field strength along the plasma plume. This method is based on the Stark shifting of the helium 492.2 nm (4^1D–2^1P) allowed line and its forbidden component (4^1F–2^1P) developed by Kuraica & Konjević (1997) as adaptions of calculations by Foster (1927). The separation between the allowed and forbidden peak, $\Delta\lambda_{pp}$, can be used to obtain a value for the electric field using (3.1) (Cvetanović *et al.* 2015). This equation is valid for electric field values in the range 3–100 kV cm^{-1}.

$$E[\mathrm{kV\,cm^{-1}}] = (-58.577 + 18.116 \times \Delta\lambda_{pp} + 3130.96 \times \Delta\lambda_{pp}^2 + 815.6 \times \Delta\lambda_{pp}^3)^{0.5}, \tag{3.1}$$

where $\Delta\lambda_{pp}$ is in nm. A schematic of the optical set-up used is shown in figure 3. The apparatus used four lenses in order to reduce vignetting and achieve a clear 1:1 object–image projection of the emitted light from the plasma plume onto the slit of a double grating spectrometer (SPEX 750) which contains $2 \times 1200\,\mathrm{l\,mm^{-1}}$ gratings. The slit width was set at 50 μm, corresponding to a measured instrumental broadening of 0.029 nm. A periscope assembly rotated the image presented to the spectrometer so that the resulting spatial information represented a radial sample across the plasma plume. A linear polarizer was placed before the entrance of the spectrometer allowing only π-polarized light to be transmitted, hence only the axial electric field is measured. An iCCD camera (Andor iStar) with 1024 × 1024 pixels, of 13 μm pixel dimension, was used

https://doi.org/10.1017/S0022377822000538 Published online by Cambridge University Press

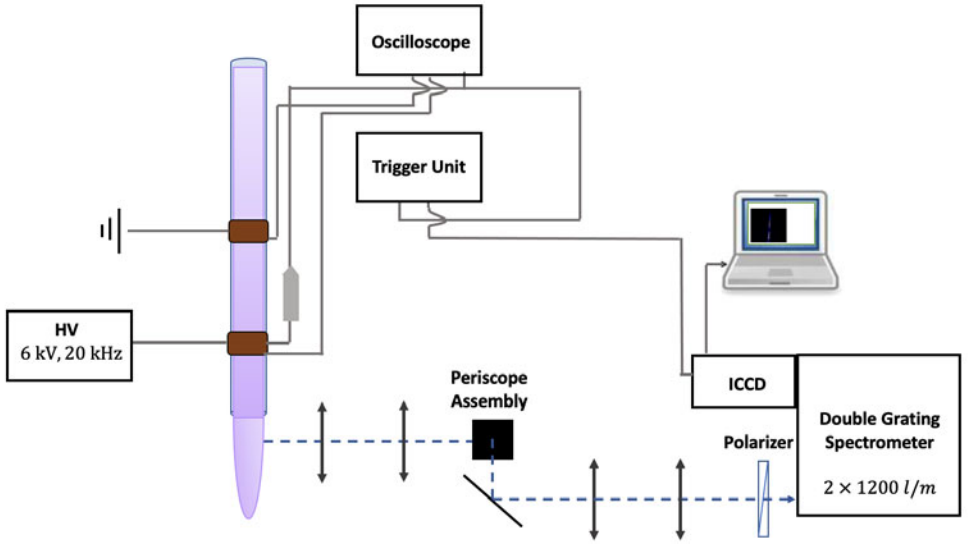

FIGURE 3. Schematic of the experimental apparatus used for obtaining axial electric field measurements of the plasma plume. A polarizer is placed in front of the spectrometer to allow only π-polarized light to be transmitted.

to capture the spectrum. The achieved spectral dispersion was 7.41 pm pixel^{-1} and the spatial resolution was 100 μm. The iCCD gate was triggered by the rising edge of the voltage pulse with a tuneable delay and adjusted to capture the plasma bullets in the field of view. Each measurement consists of 150 accumulations, each with 2×10^7 gates of 25 ns duration. The plasma jet source was moved vertically upwards in 1 mm increments using a motorized controller and the timing adjusted accordingly to follow the plasma bullets along the plasma plume.

For each of the recorded spectra at the imaged plume positions, a lineout along the same region of interest was taken. This lineout was taken centrally along the $z = 0$ axis of the plume and had a spatial size of 0.8 mm. The electric field values measured in this way correspond to those at the luminous head of the plasma bullet along this central region of interest, hence they represent the average electric field measured and do not contain information regarding its radial profile. Upon exiting the tube, it is known that the plasma bullets electric field profile is initially annular and becomes spherical further along the plume due to air diffusion into the helium gas flow (Sretenović *et al.* 2011; Naidis 2012). This annular bullet profile is initially evident in the recorded spectrum upon exiting the tube, however, it typically changes 2–5 mm after the tube exit into a spherical profile, depending on the helium flow rate.

A typical output spectrum taken from a lineout of the iCCD image is shown in figure 4. There are 3 main contributions; the 492.2 nm allowed line, its forbidden component and emission from a molecular nitrogen second positive system transition (SPS) at 491.7 nm. Transitions of both the helium and nitrogen (SPS) appear predominantly through excitation by energetic electrons (Sretenovic *et al.* 2012). All of these peaks must be accounted for in the fitting process to allow an accurate value of $\Delta\lambda_{pp}$ to be obtained. Typically, instrumental broadening and Doppler broadening have a Gaussian profile whereas Stark broadening and van der Waals broadening are Lorentzian, so an overall Voigt line profile is expected. Since the jet operates at atmospheric pressure, Doppler broadening due to

https://doi.org/10.1017/S0022377822000538 Published online by Cambridge University Press

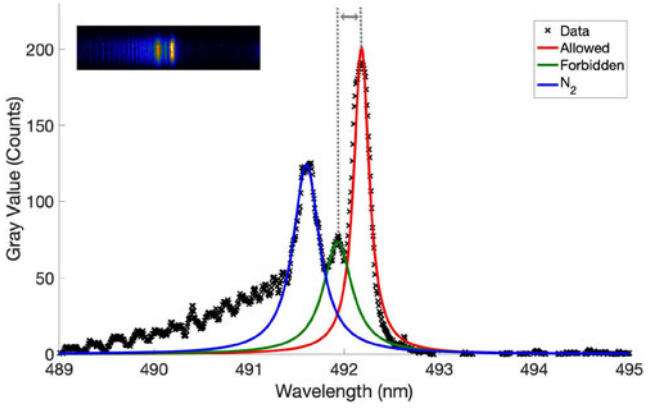

FIGURE 4. Data taken from a lineout across the inset (top left) with all contributing components fitted with pseudo-Voigt profiles. The grey dotted line represents separation between the allowed and forbidden peaks, $\Delta\lambda_{pp}$.

high temperature discharges are unlikely and can be neglected. Each line was fitted with a pseudo-Voigt profile taking into account the instrumental broadening. The separation, $\Delta\lambda_{pp}$, between the allowed and forbidden peaks was then substituted into (3.1) to calculate the corresponding field strength.

Figure 5 shows the axial electric field measured for different gas flow rates along the length of the plasma plume at a supplied voltage of 6 kV. The jet can be seen in the laboratory to extend a few mm further than the maximum distances shown in the figure, however, there is insufficient emitted light intensity in this region for useful measurements. The visible tip of the plume also experiences turbulence, causing the length of the plume to fluctuate in the mm range and making measurements in this region impractical. The strength of the electric field is shown to increase gradually as a function of distance along the plume length. The general behaviour of increasing electric field remains the same for all gas flows, with the main difference being that, at lower flows, the electric field rises at a quicker rate along the plume in comparison with higher flows with the overall range of the electric field profile being similar in magnitude. This relationship of increasing electric field strength with increasing distance along the plume has been observed for similar plasma jets (Sretenović *et al.* 2014; Sobota *et al.* 2016; Kovačević *et al.* 2018; Hofmans & Sobota 2019). This gradual increase seen for all flows comes partly as a result of the radial size of the plasma bullet decreasing with distance. This causes an increase in charge density resulting in a higher electric field. Experiments and numerical simulations have demonstrated that the electron density increases along the path of the plume consistent with the increasing electric field values (Naidis 2012; Klarenaar *et al.* 2018; Kovačević *et al.* 2018; Hofmans *et al.* 2020). The difference for the rate of increase of electric field strength seen for the different gas flows comes largely due to gas mixing of the helium with the surrounding air. To further demonstrate this gas mixing, schlieren imaging was used to visually investigate the fluid dynamics between the pure flowing helium and surrounding air. The optical arrangement consisted of two 300 mm focal length lenses, a white light source, a razor blade and an iCCD camera. The blade was positioned vertically at the focal point of the second lens. A final lens was placed in front of the camera to improve image quality. The exposure time of each image was 50 µs. Figure 6 shows images captured of the helium flow. As can be seen, there is a clear difference in the flowing helium shape and in its mixing with the ambient air for the two helium flow rates. At 2 slm, the helium flow

https://doi.org/10.1017/S0022377822000538 Published online by Cambridge University Press

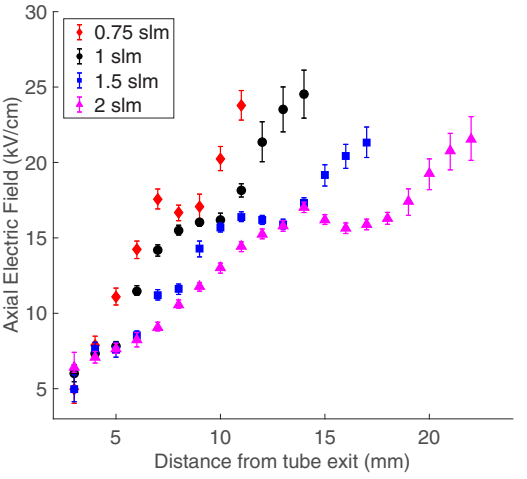

FIGURE 5. Variation of the axial electric field along the plume for different helium flow rates. (6 kV, 20 kHz).

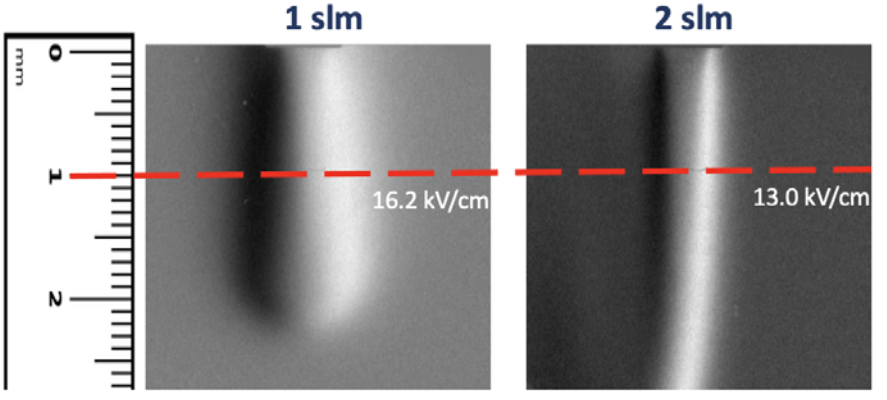

FIGURE 6. Schlieren images of the helium flow upon exiting the quartz tube for flow rates of 1 and 2 slm. The red dashed line represents a distance of 10 mm from the tube exit. The measured axial electric field values at these planes are shown.

is almost completely laminar across the region imaged, whereas at 1 slm, the helium gas expands radially with distance along the plume and diffuses into the air. Since the plasma discharge propagates along a helium–air channel upon exiting the tube, more mixing of the helium with the surrounding air will result in a higher molar fraction of air along the propagation channel. At 10 mm from the tube exit, the measured electric field at 1 slm is 3.2 kV cm^{-1} greater than that measured at 2 slm. The greater helium–air mixing for a 1 slm flow rate is readily visible at the position of the dashed line in figure 6. The value of the first Townsend ionization coefficient for discharge propagation is lower for a helium–air channel in comparison with pure helium, therefore, a greater fraction of air in the helium flow will reduce this coefficient, resulting in an increased electric field (Sobota *et al.* 2016; Kovačević *et al.* 2018), as also observed in numerical simulations (Naidis 2012; Hofmans *et al.* 2020).

https://doi.org/10.1017/S0022377822000538 Published online by Cambridge University Press

Since the applications of the plasma jet requires it to be impacting on a target, it is important to know what changes this will have on the dynamics of the jet. Any object in the close vicinity of the plasma plume will have an effect on it because it will divert the gas flow and interact electrically with the plasma. For example, if an object is placed slightly beyond the visible plume length of the plasma, the plume will extend further to make contact with the surface of the object. To get a better understanding of targets and how their dielectric or conductive properties plus their distance from the tube exit influences the plasma, the electric field profile along the jet was studied for two different targets; plastic and water. Three distances between the tube exit and target were investigated; 8, 14 and 16 mm, as shown in figure 7. Neither target was grounded for these measurements. For both targets, there are minimal changes in the measured electric field except at a few mm directly above the target where a clear enhancement can be observed. The magnitude of this increase is strongly dependent on the distance between the tube exit and the target. When the target was placed 8 mm from the tube exit, an increase of $0.9\,\mathrm{kV\,cm^{-1}}$ (relative increase of 6 %) is measured for plastic and $1.5\,\mathrm{kV\,cm^{-1}}$ (relative increase of 10 %) for water in comparison with that measured for a freely expanding jet at the same position. However, when the target distance was extended to 14 mm, an increase of $4.0\,\mathrm{kV\,cm^{-1}}$ (relative increase of 16 %) is measured for plastic and $6.8\,\mathrm{kV\,cm^{-1}}$ (relative increase of 28 %) for water. When the target distance was extended another 2 mm from the tube exit, the electric field increased further, reaching as high as $31.2 \pm 2.3\,\mathrm{kV\,cm^{-1}}$ for plastic and $32.1 \pm 1.6\,\mathrm{kV\,cm^{-1}}$ for water. Whilst no electric field measurement was taken at this distance for the freely expanding jet due to low signal, from figure 7(*c*), a notable increase can already be seen for both targets at 14 mm, therefore, we postulate that the electric field measured for both targets at 15 and 16 mm is greater than that for a freely expanding jet.

This behaviour of additional electric field enhancement depending on the target position is again partly related to the fraction of air due to mixing, outlined previously. Figure 7(*d*), displays the targets positions overlayed on a schlieren image of the helium flow when no plasma was ignited. There is a greater diffusion of helium into the surrounding air along the planes (*b*,*c*) in comparison with plane (*a*). This means greater gas mixing at these planes resulting in a higher molar fraction of air present and hence a higher electric field. Another contributing factor leading to the electric field enhancement is due to the compression of charge on striking the target surface. Figure 8 shows images of the plasma plume interacting with the plastic and water target at the measured positions. It can be seen that the larger the separation between the tube exit and target, the more constricted the plasma plume becomes at the surface of the target, which would lead to compression of charge and hence a higher electric field. One main difference between the two targets is a radial spreading of the plasma on the surface of the plastic target covering a much larger surface area of the target in comparison with water. The slight additional enhancement of the electric field for the water target may partially be due to charging of the surface on impact. Numerical simulations of a similar gas jet interacting with targets of varying permittivities showed that higher permittivity targets resulted in more positive charge build up on the target surface (Viegas & Bourdon 2020). This behaviour of different targets only inducing enhanced peak electric fields near the target has been seen both experimentally (Klarenaar *et al.* 2018; Sobota *et al.* 2019) and numerically (Norberg, Johnsen & Kushner 2015; Wang, Zheng & Jia 2016; Ji *et al.* 2018; Schweigert *et al.* 2019). Thomson scattering measurements of a similar gas jet impacting upon different targets also show the electron density increasing with distance from the tube exit, reaching a higher maximum electron density immediately before the target (Klarenaar *et al.* 2018), with a larger increase in electron density for conducting targets of copper and water in comparison with glass. This increase in electron density would result in a higher electric field. Therefore the additional

https://doi.org/10.1017/S0022377822000538 Published online by Cambridge University Press

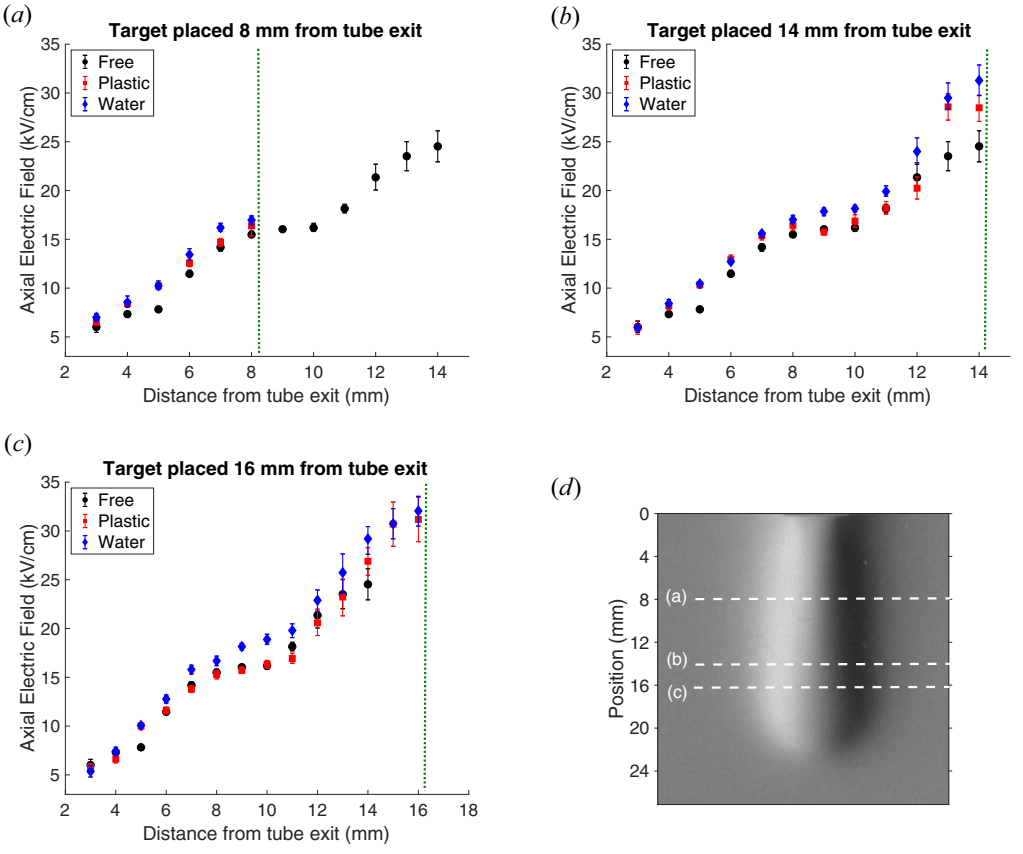

FIGURE 7. Comparison of the axial electric field profile along the plasma plume for a freely expanding jet and for the jet interacting with a target of plastic and water placed at a distance of (*a*) 8 mm, (*b*) 14 mm and (*c*) 16 mm. (*d*) Target positions overlayed on schlieren image of the helium flowing at 1 slm (no plasma ignited).

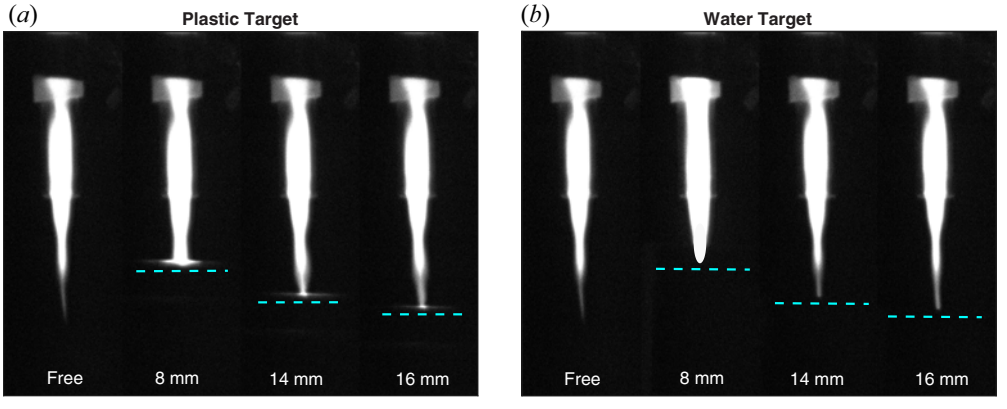

FIGURE 8. Images of the plasma–target interaction at different target positions for (*a*) plastic and (*b*) water.

https://doi.org/10.1017/S0022377822000538 Published online by Cambridge University Press

increase in density measured for conducting targets would explain why our electric field magnitude is on average greater for water compared with plastic.

3.2. *Fast two-dimensional monochromatic imaging*

In order to estimate excited state densities within the plasma jet, a fast two-dimensional (2-D) monochromatic imaging configuration was utilized to measure emission from the plasma source quartz tube. This required imaging the plasma bullets with an appropriate bandpass filter attached to the iCCD to isolate emission from single states. A 200 mm focal length lens was used and an appropriate filter mounted to the iCCD. The camera was triggered by the rising edge of the voltage pulse in a similar manner to that described in § 3.1. The gate time used was 20 ns and each exposure resulted in an accumulation of 10 bullets per image. The propagation of the plasma bullets were recorded at 50 ns intervals. Due to the strong emission intensity of helium lines shown in figure 1(*b*), the helium ^{3}S at 706.5 nm and ^{1}S at 728.1 nm were chosen to investigate. Sample images of the plasma bullets within the source can be seen in figure 9(*a*). These are 2-D images of 3-D plasma bullets, however, assuming the bullet is an optically thin plasma, the signal in each pixel corresponds to the line integrated emission from excited helium states in a column extending from the pixel through the plasma bullet to infinity. The emission value recorded at each pixel is therefore the emission integrated along a column with face area equal to the pixel width squared, w_{px}^2. For each image, a lineout along the bullet region was taken, as shown in figure 9(*b*). The measured profile is reasonably approximated, for our purposes, by a Gaussian. If each pixel corresponds to the total emission from helium states in a long column extending through that pixel, we can relate the maximum signal, C_p, per bullet, taken here as the amplitude of the Gaussian fit divided by the number of bullets accumulated on the camera, to the total number of emitters, N_{em}, in that column using (3.2)

$$N_{\mathrm{em}} = \frac{4\pi C_p}{E_\gamma \times \mathrm{iCCD_{res}} \times \mathrm{QE} \times T \times \Omega}. \tag{3.2}$$

Here, $\mathrm{iCCD_{res}}$, is the response of the iCCD and has units of counts/eV, E_γ is the photon energy of the transition being observed and QE is the quantum efficiency of the iCCD, i.e. the fraction of photons incident on the CCD that are absorbed and contribute to the pixel signal. Also, T is the total transmission of the imaging system and is dominated by the transmission of the bandpass filter and Ω is the solid angle subtended by the first lens in the imaging system. The response of the iCCD was initially calibrated for each bandpass filter before taking any measurements. The bandpass filters used were 700 and 730 nm (Thorlabs FB700-10 and FL730-10), both having a full width at half-maximum (FWHM) of 10 ± 2 nm, thus allowing emission from ^{3}S and ^{1}S states to pass through the given filter. Transmission profiles over the wavelength range of the filters were provided by the supplier, however, due to the uncertainty of the central wavelength of each filter, ± 2 nm, the quoted transmissions were experimentally verified. The numerical values used in the analysis are tabulated in table 1.

The radial density profile of the excited helium states corresponding to the transition we are observing, $n_{\mathrm{He}}(r)$, must firstly be obtained. The shape of this profile will be the Abel inversion of the profile projected onto the camera, i.e. the lineout along the region of interest. Since this is well fitted by a Gaussian, we can take the Abel inversion to also be a Gaussian with the same FWHM. Assuming that the density does not significantly vary during the exposure time, t, for any single bullet the number of emitters is approximated

https://doi.org/10.1017/S0022377822000538 Published online by Cambridge University Press

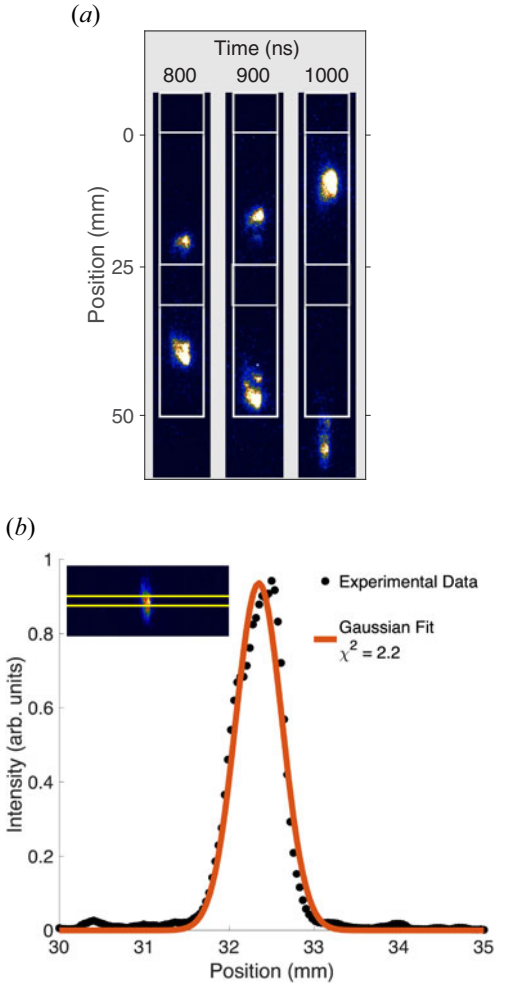

FIGURE 9. (*a*) Sample images of the plasma bullets at 3 different time delays when the 700 nm bandpass filter was present. The powered electrode extends from 25 to 30 mm and the ground electrode from −5 to 0 mm. (*b*) Data taken from a lineout across the plasma bullet region (inset) fitted using a Gaussian profile with $\chi^2 = 2.2$.

	706 nm	728 nm
$iCCD_{res}$ (Counts/eV)	383	189
E_γ (eV)	1.76	1.70
QE of ICCD (%)	21.4	10.5
Bandpass Filter Transmission (%)	21.7	78.9
A-rates, A_{ul} (s^{-1})	2.79×10^7	1.83×10^7
Degeneracy	3	1

TABLE 1. Values used to calculate the excited state densities of the helium ^3S and ^1S states.

https://doi.org/10.1017/S0022377822000538 Published online by Cambridge University Press

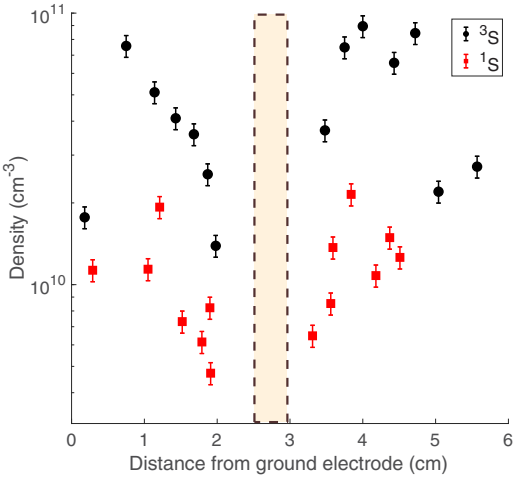

FIGURE 10. Excited state densities of the ^{3}S at 706 nm and ^{1}S at 728 nm helium states as a function of distance from the grounded electrode. The brown dashed rectangle represents the position of the powered electrode.

by (3.3)

$$A_{ul}w_{\mathrm{px}}^2\int_0^t\int_{-\infty}^{\infty} n_{\mathrm{He}}(r)\,\mathrm{d}r\,\mathrm{d}t = A_{ul}w_{\mathrm{px}}^2 t2\int_0^{\infty} n_{\mathrm{He}}(r)\,\mathrm{d}r \approx N_{\mathrm{em}}, \tag{3.3}$$

where A_{ul}, is the rate at which the excited states emit. The A rates are transition dependent and since the 706 nm helium state has a degeneracy of $g = 3$, the sum of the three A rates was used. The values of the A rates were taken from NIST Atomic Spectra Database (Kramida *et al.* 2021) and are also tabulated in table 1. The time is dictated by the camera acquisition and was 20 ns for all images. In figure 9(*a*), two distinct sets of plasma bullets can be seen in each image, one of the bullets travelling upwards starting from the powered electrode towards the ground electrode, and the other again starting from the powered electrode but travelling downwards towards the open end of the quartz tube with little emission being detected outside of the tube. Figure 10 compares the excited state densities of the ^{3}S and ^{1}S helium states. For both states and bullet propagation directions, the excited state density is lowest at the point of creation (the powered electrode) and shows an increase with distance from the powered electrode before decreasing again. The measured excited state density for the ^{3}S state is on average much larger than the ^{1}S state, reaching a maximum density of up to $(9.0 \pm 0.8) \times 10^{10}$ cm^{-3} for the ^{3}S state and $(3.4 \pm 0.3) \times 10^{10}$ cm^{-3} for the ^{1}S state. For both states there was little to no detection of emission along the plume upon exiting the tube. This most likely comes as a result of helium quenching through Penning ionization from the increased fraction of oxygen outside of the tube. One study conducted on a helium radio frequency-driven APPJ using a collisional–radiative model to estimate helium and oxygen excited state densities as a function of relative air concentration showed that both the ^{3}S and ^{1}S helium excited state densities decreased rapidly for air concentrations above 0.1 % (Petrova *et al.* 2020).

4. Conclusions

Several optical diagnostics were utilized to investigate the behaviour of a kHz APPJ source. Electric field measurements made along the length of the plume showed that the electric field increases with distance from the tube exit. These values ranged from 4 to

https://doi.org/10.1017/S0022377822000538 Published online by Cambridge University Press

25 kV cm^{-1}. This increase comes as a result of the plasma bullets radially decreasing in size as a function of distance from the tube exit meaning the field lines will also be compressed. The rate of increase has been shown to be dependent on the helium gas flow rate, with lower gas flows showing a sharper increase with distance in comparison with larger flow rates with the typical values measured remaining within the same range. Schlieren imaging was used to demonstrate this difference by showing that a greater fraction of air mixed in the helium flow resulted in a higher electric field. The presence of a target was shown to influence the magnitude of the electric field in close proximity to the target. The magnitude of this increase is strongly dependent on the distance between the tube exit and the target, with larger separation causing a greater relative change in the measured electric field. The relative increase measured was on average higher for the conducting target of water compared with plastic. A cheap minimal equipment optical measurement configuration, termed here as fast 2-D monochromatic imaging, was introduced as a tool for measuring excited state densities within the plasma jet source. Using this method, estimates for the excited helium ^{3}S and ^{1}S states inside the source were found to be of the order of 10^{10}–10^{11} cm^{-3}.

Acknowledgements

We would like to acknowledge Dr C.M.O. Mahony for his useful feedback on this manuscript and the referees for their remarks and advice.

Editor Edward Thomas, Jr. thanks the referees for their advice in evaluating this article.

Funding

This research was funded by Engineering and Physical Sciences Research Council (EPSRC), grant number EP/P026079/1.

Declaration of interests

The author report no conflict of interest.

REFERENCES

Akishev, Y.S., Karalnik, V.B., Medvedev, M.A., Petryakov, A.V., Trushkin, N.I. & Shafikov, A.G. 2017 Influence of DC and AC external electric field on the propagation of plasma bullets along DBD helium plasma jet. *J. Phys.: Conf. Ser.* **927**, 12051.

Attri, P., Ishikawa, K., Okumura, T., Koga, K. & Shiratani, M. 2020 Plasma agriculture from laboratory to farm: a review. *Processes* **8** (8).

Beebe, S.J., Blackmore, P.F., White, J., Joshi, R.P. & Schoenbach, K.H. 2004 Nanosecond pulsed electric fields modulate cell function through intracellular signal transduction mechanisms. *Physiol. Meas.* **25** (4), 1077–1093.

Cvetanović, N., Martinović, M.M., Obradović, B.M. & Kuraica, M.M. 2015 Electric field measurement in gas discharges using stark shifts of He i lines and their forbidden counterparts. *J. Phys.* D*: Appl. Phys.* **48**.

Flynn, P.B., Busetti, A., Wielogorska, E., Chevallier, O.P., Elliott, C.T., Laverty, G., Gorman, S.P., Graham, W.G. & Gilmore, B.F. 2016 Non-thermal plasma exposure rapidly attenuates bacterial AHL-dependent quorum sensing and virulence. *Sci. Rep.* **6** (1), 1–13.

Foster, J.S. 1927 Stark Patterns Observed in Helium. *Proc. R. Soc.* A **114**, 47–66.

Georgescu, N., Lungu, C.P., Lupu, A.R. & Osiac, M. 2010 Atomic oxygen maximization in high-voltage pulsed cold atmospheric plasma jets. *IEEE Trans. Plasma Sci.* **38** (11), 3156–3162.

Hofmans, M. & Sobota, A. 2019 Influence of a target on the electric field profile in a kHz atmospheric pressure plasma jet with the full calculation of the Stark shifts. *J. Appl. Phys.* **125** (4), 043303.

Hofmans, M., Viegas, P., van Rooij, O., Klarenaar, B., Guaitella, O., Bourdon, A. & Sobota, A. 2020 Characterization of a kHz atmospheric pressure plasma jet: comparison of discharge propagation parameters in experiments and simulations without target. *Plasma Sources Sci. Technol*. **29** (3), 34003.

Ji, L., Yan, W., Xia, Y. & Liu, D. 2018 The effect of target materials on the propagation of atmospheric-pressure plasma jets. *J. Appl. Phys*. **123** (18), 183302.

Kim, S. J., Chung, T.H., Bae, S.H. & Leem, S.H. 2010 Induction of apoptosis in human breast cancer cells by a pulsed atmospheric pressure plasma jet. *Appl. Phys. Lett*. **97**, 023702.

Klarenaar, B.L.M., Guaitella, O., Engeln, R. & Sobota, A. 2018 How dielectric, metallic and liquid targets influence the evolution of electron properties in a pulsed He jet measured by Thomson and Raman scattering. *Plasma Sources Sci. Technol*. **27** (8), 85004.

Kong, M.G., Kroesen, G., Morfill, G., Nosenko, T., Shimizu, T., van Dijk, J. & Zimmermann, J.L. 2009 Plasma medicine: an introductory review. *New J. Phys*. **11** (11), 115012.

Kovačević, V.V., Sretenović, G.B., Slikboer, E., Guaitella, O., Sobota, A. & Kuraica, M.M. 2018 The effect of liquid target on a nonthermal plasma jet imaging, electric fields, visualization of gas flow and optical emission spectroscopy. *J. Phys.* D*: Appl. Phys*. **51** (6), 65202.

Kramida, A., Ralchenko, Y., Reader, J. & NIST ASD Team 2021 NIST Atomic Spectra Database (ver. 5.9), [Online]. Available: https://physics.nist.gov/asd [2022, Feb 1]. National Institute of Standards and Technology.

Kuraica, M.M. & Konjević, N. 1997 Electric field measurement in the cathode fall region of a glow discharge in helium. *Appl. Phys. Lett*. **70**, 1521–1523.

Laroussi, M., Kong, M., Morfill, G. & Stolz, W. 2012 *Plasma Medicine: Applications of Low-Temperature Gas Plasmas in Medicine and Biology*, pp. 156–174. Cambridge University Press.

Lu, X., Naidis, G.V., Laroussi, M. & Ostrikov, K. 2014 Guided ionization waves: theory and experiments. *Phys. Rep.* **540**.

Moreau, M., Orange, N. & Feuilloley, M.G.J. 2008 Non-thermal plasma technologies: new tools for bio-decontamination. *Biotechnol. Adv*. **26** (6), 610–617.

Naidis, G.V. 2012 Modeling of helium plasma jets emerged into ambient air: Influence of applied voltage, jet radius, and helium flow velocity on plasma jet characteristics. *J. Appl. Phys*. **112** (10), 103304.

Norberg, S.A., Johnsen, E. & Kushner, M.J. 2015 Helium atmospheric pressure plasma jets touching dielectric and metal surfaces. *J. Appl. Phys*. **118** (1), 013301.

Nuccitelli, R., Pliquett, U., Chen, X., Ford, W., Swanson, R.J., Beebe, S.J., Kolb, J.F. & Schoenbach, K.H. 2006 Nanosecond pulsed electric fields cause melanomas to self-destruct. *Biochem. Biophys. Res. Commun*. **343** (2), 351–360.

Park, G.Y., Park, S.J., Choi, M.Y., Koo, I.G., Byun, J.H., Hong, J.W., Sim, J.Y., Collins, G.J. & Lee, J.K. 2012 Atmospheric-pressure plasma sources for biomedical applications. *Plasma Sources Sci. Technol*. **21** (4), 043001.

Pei, X., Wu, S., Xian, Y., Lu, X. & Pan, Y. 2014 On OH density of an atmospheric pressure plasma jet by laser-induced fluorescence. *IEEE Trans. Plasma Sci*. **42** (5), 1206–1210.

Petrova, T.B., Boris, D.R., Hinshelwood, M., Johnson, M.J., Gillman, E.D. & Walton, S.G. 2020 Helium and oxygen excited states densities in a He-air RF-driven atmospheric pressure plasma jet. *Phys. Plasmas* **27** (10), 103512.

Schröter, S., Bredin, J., Gibson, A.R., West, A., Dedrick, J.P., Wagenaars, E., Niemi, K., Gans, T. & O'Connell, D. 2020 The formation of atomic oxygen and hydrogen in atmospheric pressure plasmas containing humidity: picosecond two-photon absorption laser induced fluorescence and numerical simulations. *Plasma Sources Sci. Technol*. **29** (10), 105001.

Schweigert, I.V., Vagapov, S., Lin, L. & Keidar, M. 2019 Enhancement of atmospheric plasma jet–target interaction with an external ring electrode. *J. Phys.* D*: Appl. Phys*. **52** (29), 295201.

Sobota, A., Guaitella, O., Sretenović, G.B., Kovačević, V.V., Slikboer, E., Krstić, I.B., Obradović, B.M. & Kuraica, M.M. 2019 Plasma-surface interaction: dielectric and metallic targets and their influence on the electric field profile in a kHz AC-driven He plasma jet. *Plasma Sources Sci. Technol*. **28** (4), 045003.

Sobota, A., Guaitella, O., Sretenović, G.B., Krstić, I.B., Kovačević, V.V., Obrusník, A., Nguyen, Y.N., Zajíčková, L., Obradović, B.M. & Kuraica, M.M. 2016 Electric field

measurements in a kHz-driven He jet the influence of the gas flow speed. *Plasma Sources Sci. Technol*. **25** (6), 065026.

Sretenović, G.B., Krstić, I.B., Kovačević, V.V., Obradović, B.M. & Kuraica, M.M. 2011 Spectroscopic measurement of electric field in atmospheric-pressure plasma jet operating in bullet mode. *Appl. Phys. Lett*. **99** (16), 161502.

Sretenovic, G.B., Krstic, I.B., Kovacevic, V.V., Obradovic, B.M. & Kuraica, M.M. 2012 Spectroscopic study of low-frequency helium DBD plasma jet. *IEEE Trans. Plasma Sci*. **40** (11), 2870–2878.

Sretenović, G.B., Krstić, I.B., Kovačević, V.V., Obradović, B.M. & Kuraica, M.M. 2014 Spatio-temporally resolved electric field measurements in helium plasma jet. *J. Phys.* D*: Appl. Phys*. **47** (10), 102001.

Steuer, D., Korolov, I., Chur, S., Schulze, J., Schulz-von der Gathen, V., Golda, J. & Böke, M. 2021 2D spatially resolved O atom density profiles in an atmospheric pressure plasma jet: from the active plasma volume to the effluent. *J. Phys.* D*: Appl. Phys*. **54** (35), 355204.

Urabe, K., Morita, T., Tachibana, K. & Ganguly, B.N. 2010 Investigation of discharge mechanisms in helium plasma jet at atmospheric pressure by laser spectroscopic measurements. *J. Phys.* D*: Appl. Phys*. **43** (9), 095201.

van Gessel, A.F.H., Alards, K.M.J. & Bruggeman, P.J. 2013 NO production in an RF plasma jet at atmospheric pressure. *J. Phys.* D*: Appl. Phys*. **46** (26), 265202.

Viegas, P. & Bourdon, A. 2020 Numerical study of jet–target interaction: influence of dielectric permittivity on the electric field experienced by the target. *Plasma Chem. Plasma Process*. **40** (3), 661–683.

Viegas, P., Hofmans, M., van Rooij, O., Obrusník, A., Klarenaar, B.L.M., Bonaventura, Z., Guaitella, O., Sobota, A. & Bourdon, A. 2020 Interaction of an atmospheric pressure plasma jet with grounded and floating metallic targets: simulations and experiments. *Plasma Sources Sci. Technol*. **29** (9), 095011.

Walsh, J.L., Iza, F., Janson, N.B., Law, V.J. & Kong, M.G. 2010 Three distinct modes in a cold atmospheric pressure plasma jet. *J. Phys.* D*: Appl. Phys*. **43** (7), 075201.

Wang, L., Zheng, Y. & Jia, S. 2016 Numerical study of the interaction of a helium atmospheric pressure plasma jet with a dielectric material. *Phys. Plasmas* **23** (10), 103504.

Wielogorska, E., Ahmed, Y., Meneely, J., Graham, W.G., Elliott, C.T. & Gilmore, B.F. 2019 A holistic study to understand the detoxification of mycotoxins in maize and impact on its molecular integrity using cold atmospheric plasma treatment. *Food Chem*. **301**, 125281.

Wu, S., Lu, X. & Pan, Y. 2013 Effects of seed electrons on the plasma bullet propagation. *Curr. Appl. Phys*. **13**, S1–S5.

Xian, Y., Lu, X., Cao, Y., Yang, P., Xiong, Q., Jiang, Z. & Pan, Y. 2009 On plasma bullet behavior. *IEEE Trans. Plasma Sci*. **37** (10), 2068–2073.

Xiong, Q., Yang, Z. & Bruggeman, P.J. 2015 Absolute OH density measurements in an atmospheric pressure dc glow discharge in air with water electrode by broadband UV absorption spectroscopy. *J. Phys.* D*: Appl. Phys*. **48** (42), 424008.

Yonemori, S. & Ono, R. 2014 Flux of OH and O radicals onto a surface by an atmospheric-pressure helium plasma jet measured by laser-induced fluorescence. *J. Phys.* D*: Appl. Phys*. **47** (12), 125401.

Zaplotnik, R., Bišćan, M., Popović, D., Mozetič, M. & Milošević, S. 2016 Metastable helium atom density in a single electrode atmospheric plasma jet during sample treatment. *Plasma Sources Sci. Technol*. **25** (3), 035023.

Zhang, Q., Zhuang, J., von Woedtke, T., Kolb, J.F., Zhang, J., Fang, J. & Weltmann, K. 2014 Synergistic antibacterial effects of treatments with low temperature plasma jet and pulsed electric fields. *Appl. Phys. Lett*. **105** (10), 104103.